

# Fast measurement of angular velocity in air-driven flat rotors with periodical features

Miguel Ángel López-Castaño<sup>a</sup>, Alejandro Márquez Seco<sup>b</sup>, Alicia Márquez Seco<sup>b</sup>, Álvaro Rodríguez-Rivas<sup>c</sup>, Francisco Vega Reyes<sup>b</sup>

<sup>a</sup>*Departamento de Física Aplicada, Centro Universitario de Mérida, Universidad de Extremadura, 06800 Mérida, Spain*

<sup>b</sup>*Departamento de Física and Instituto de Computación Científica Avanzada (ICCAEx), Universidad de Extremadura, Avda. Elvas s/n, 06071 Badajoz, Spain*

<sup>c</sup>*Department of Physical, Chemical and Natural Systems, Pablo de Olavide University, 41013, Sevilla, Spain*

---

## Abstract

We present a method for resolving 2D angular movement in a set of particles provided with periodical features. The main advantage of the base algorithm in our method lies in its low computational complexity while displaying a relatively high accuracy. This is specially useful in situations where real-time angular measurement is crucial, such as industrial applications. For the sake of illustration, we apply our technique to a system of active spinners thermalized with an upflow air current. We show that the proposed method allows for accurate measurement of fast dynamics features in the systems, such as rapid velocity autorrelation oscillations and particle spin average field.

*Keywords:* image processing, particle tracking, experimental, rotation, active matter

---

## 1. Introduction

Accurate measurement of particle rotation is crucial for a wide variety of applications, like characterization of collisional properties for macroscopic particles [1, 2, 3], design of microrotors properties for their use as non-invasive drug delivery vectors [4] and evaluation and calibration of rotating machinery in many industrial scenarios. In this paper we develop a *particle tracking velocimetry* (PTV) algorithm [5] based on the analysis of the particles brightness profiles from a set of digital images. The observed brightness profiles reproduce the periodical features of the particles, which allows for accurate measurement, as we will see, of their rotational velocity.

In previous experimental works, several methods are routinely employed to extract particle angular velocity information from a set of images. A simple approach would typically employ a stroboscope [6] or an on-board mounted sensor (tachometer) [7]. In camera-based experiments, another common approach is to analyse asymmetrical features of the particle [8] or to put a tracer mark on the particle [9, 10]. Angular displacements are followed in this case by measuring the mark angle relative to a fixed axis which passes through the particle center. This method requires identification of two points: particle center and mark position. In the case of spheres, more complex methods have been described [11, 12, 13], often making use of twin cameras to obtain a three dimensional perspective [14].

However, depending on the experimental conditions, particle marking might not be feasible. Thus, it is useful

to develop a method which does not require particle markers. For instance, one such method consists in looking at the pixel intensity arrays of two consecutive frames [15, 16]. These two frames are iteratively cross-correlated [17], each step rotating the second array a certain angle. This operation results in a probability distribution of scalar coefficients indicating the similarity between the original first frame and the rotated second frame. The corresponding maximum likelihood estimate of a Gaussian signals the true angular displacement. This method has the drawback that computing time quickly increases for increasing accuracy, which implies smaller angle step iteration (since cross correlation computation is time consuming) [16].

For this reason, we propose an alternate method that is based on a significantly faster algorithm. Our method can be applied to systems composed of particles provided with periodically spaced identical features. In our case, particles are 3D printed disks with 14 equal size blades (see Figure 2 a). The particle dynamics is generated by an air upflow (Figure 2 b). We found that our method yields a high accuracy at relatively low computational cost. We think this is relevant, provided the relatively high data-throughput of modern PTV and imaging systems [18]. This work is organized as follows: in the next section we provide a brief description of the experimental system; in Section 3, a step by step description of the algorithm is provided, along with some measurements regarding its accuracy, errors and computational advantages; finally in Section 4 we analyze the output produced by this technique from measurements of the rotation on a the set of active spinners. For this final task, several series of experiments at different particle density and driving upflow

---

*Email address:* malopez00@unex.es (Miguel Ángel López-Castaño)

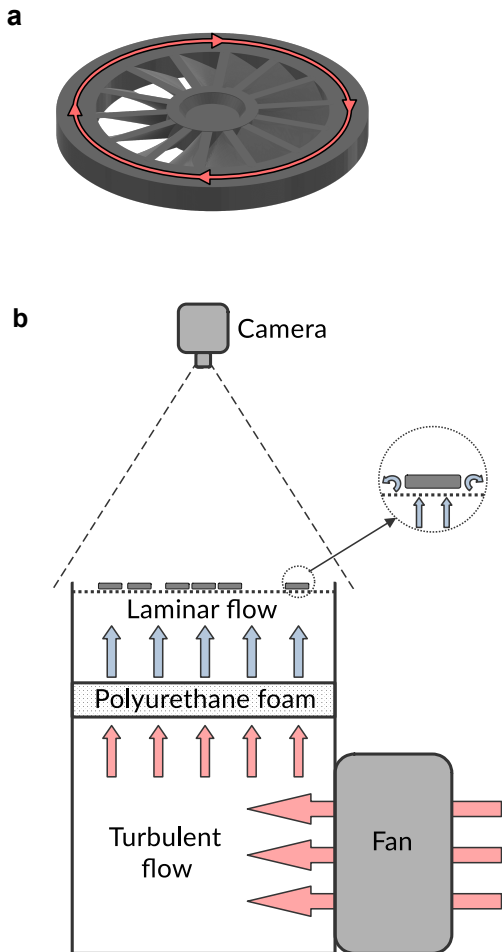


Figure 1: (a) 3D render of a CW rotating disk. A total of 14 oblique blades enable particle spinning under the action of an impinging air flow. (b) Sketch of the experimental device.

intensity are taken.

## 2. Description of the system

A diagram of the set-up is shown in Figure 1. We employ a variable number  $N$  of identical disks with diameter  $\sigma = 72.5 \pm 0.1$  mm. The disk thickness is  $h = 6 \pm 0.1$  mm and its mass  $m = 7.76 \pm 0.10$  g. They are made of polylactic acid (PLA) and have been fabricated using additive 3D printing (.stl models are available upon request). As we said, each disk is provided with a set of equally-spaced identical blades (Figure 1a). However, the moment of inertia of the particles can be approached by the value corresponding to a flat solid disk with homogeneous density. Taking into account the values of our PLA particles mass and diameter, then we obtain  $I \simeq (1/8) m \sigma^2 \simeq 51$  g/cm<sup>2</sup>. The disks are placed on a perforated metallic grid which receives an adjustable air flow from below. See Figure 1(b) for a schematic depiction of the experimental set-up. The

upflow is adjusted so that all particles levitate at a minimum height over the grid, thus avoiding friction. Moreover, particle dynamics remains in a horizontal monolayer (and thus, 2D) at all times, which simplifies the process of particle tracking. Movement is limited to a circular region with diameter  $L = 725 \pm 1$  mm. A similar experimental configuration has been successfully employed recently in a series of experiments for studies on active particle dynamics [19, 10, 20]. In our case, system size is  $L/\sigma \simeq 10$  (sufficiently big in units of particle size for our statistical analysis). Packing fraction as  $\phi = N(\sigma/L)^2 = N/100$ .

Let us define the global averages of the particle translational and rotational thermal fluctuation energies  $\overline{T}_t = (m/2)\langle(\mathbf{v} - \mathbf{u})^2\rangle_r$ ,  $\overline{T}_r = (I/2)\langle\mathbf{w}^2\rangle_r$  respectively. The notation  $\langle \dots \rangle_r$  stands for space averaging of the magnitude inside the brackets, carried out over all particles for all recorded frames (since we only deal with steady states) in one experiment. Here,  $\mathbf{v}$  and  $\mathbf{w} = w_z \hat{\mathbf{e}}_z$  are particle velocity and angular velocity (or spin) respectively, where  $\hat{\mathbf{e}}_z$  is a unit vector perpendicular to the metallic grid and pointing upwards; and  $\mathbf{u}$  is the fluid flow (i.e., the local average of particles velocities  $\mathbf{v}$ ). It is also convenient to define the average of particle spin modulus  $\langle w \rangle_r \equiv \langle |w_z| \rangle_r$ .

Von Karman street vortices [21] past the disks produce air flow small-scale turbulence [22]. Thus, the particles acquire Brownian-like translational movement. In addition, constant upflow past the blades results in continuous particle rotation. Therefore, after a short transient, the system attains a stationary state characterized by Brownian-like particle translations and nearly constant particle spin. However, dynamic fluctuations due to small scale air turbulence are enhanced (in particle rotation rate as well) by frequent particle-particle and particle-boundary collisions (see Movie 1 in the Supplementary Material [23] for reference), which renders steady states far from equilibrium particle velocity and spin distributions [24]. We focus in this work only on these steady states.

Although we designed the disks so that airflow yields clockwise (CW) rotation ( $w_z < 0$ ), particle spin can temporarily become counter clockwise (CCW, thus  $w_z > 0$ ) [24] (see also Figure 3 c) due to disks collisions and thus our algorithm is prepared to detect both cases.

We recorded a sufficiently complete set of experiments with different densities and fan air power (which results in different degrees of particles thermalization). Each experiment has a duration of approximately 27 s and is recorded using a high-speed Phantom VEO-410L camera, at a resolution of  $1280 \times 800$  px (px stands for pixel). At our working image resolution and camera position, a pixel width is equivalent to  $1 \text{ px} = 0.9295$  mm in the horizontal plane where all the dynamics occurs.

## 3. Particle tracking and angular velocity detection method

Since particle angle is measured with respect to the particle center, as a precondition we need to achieve ac-

curate detection of particle positions (defined as the position of particle centers). This is achieved with the use of OpenCV functions [25, 26, 20]. Particle positions are detected in every frame and, for relating each particle with itself in the next frame (linking procedure [5]), we use an ad-hoc adaptation of original the PTV algorithm by Crocker and Grier [5], in its Python version [27]. This procedure allows for the determination of particle trajectories (tracks). For more details on particle tracks determination, the reader may refer to a previous work where we used and described an analogous procedure for the analysis of the 2D dynamics of a set of spheres [20].

Once we have identified and linked the particle positions for all frames, our code proceeds to particle angle detection and linkage. For this, angular displacements between consecutive frames cannot be larger than half the angle between consecutive blades. This is so because features (blades) are identical and thus if this condition were not fulfilled it would not be possible to distinguish if the blade displacement between consecutive frames occurs in one sense or the opposite (Figure 2(a) can be illustrative of this). Therefore,  $\Delta\theta_{\max} < \frac{1}{2}(2\pi/N_b)$  (where the right hand side in the inequality is exactly one half of inter-blade separation, in radians). This implies that  $\langle w \rangle_r \Delta t < \theta_{\max}$  (the term in the left is the typical blade rotation between frames at a frame rate  $1/\Delta t$ ), which yields  $\Delta t < \Delta\theta_{\max}/\langle w \rangle = (\pi/N_b)/\langle w \rangle$ . In our experiments  $\langle w \rangle \simeq 16\pi$  rad/s,  $N_b = 14$ , and thus we obtain a minimum working frame rate of 224 fps. Therefore, for particle rotation tracking we have recorded all experiments movies at 900 fps, which is well above the former limit. This is necessary for measurement of particle spin in the high rotational energy tails of the particle spin distribution (allows for measurement of up to  $\sim 32$  revolutions per second, 4 times the typical particle spin).

Our algorithm for detection of particle angular displacement works as follows:

Step 1: In every frame, we extract a brightness profile  $B_i(\theta)$  for all detected disks (with  $i = 1 \dots N_b$ ), which yields a data series with angle values in the interval  $[0, 2\pi]$ , as in Figure 2(b). This profile is obtained out of an annular section of the disk, where  $\theta$  values are measured for each pixel inside the annulus (see colored section of the disk image in Figure 2a), with respect to the disk center, as we explained. Blades positions are then identified as the maxima in these profiles. For this, we determine the corresponding intensity peaks by approximating the profile of each blade to a Gaussian distribution. In order to calculate the relative angle to the center one must avoid using the tangent function since its asymptotic behavior is undesirable. The former procedure results in an array of  $N_b$  angles  $\{\theta_i(t=0)\}$ , each corresponding to the previously determined brightness peaks (see Figure 2b).

Step 2: Next, blade angle arrays  $\{\theta_i\}$  are ordered in such

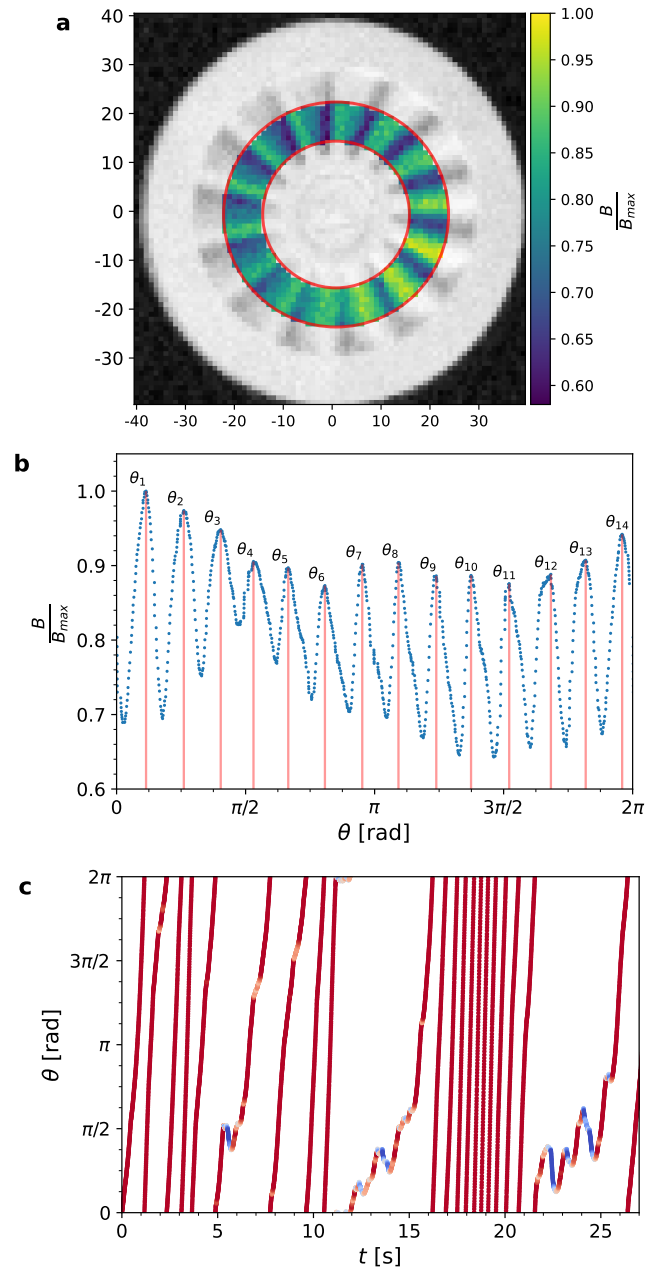


Figure 2: Processing steps. (a) Image of a single disk, axis units are in pixels. We loop across every particle in each frame. Then, an annular interest region (colored) is analyzed in order to detect the angular position of the tilted blades. (b) Distribution of pixel luminosity in the interest region, ordered by their angular position from an arbitrary axis (x- axis), from these brightness values we can extract the peaks mentioned in section 3. (c) Particle spin vs. time for a representative particle track, in an experiment with  $N = 55$  particles, at  $T_i = 0.91 m\sigma^2/s^{-2}$ . Symbol colors red and blue indicate counter clockwise and clockwise spin, respectively. Point color intensity is proportional to instantaneous angular speed, in such a way that pure white stands for zero spin. We can see that the natural rotation (counter clockwise) can momentarily be reversed (typically due to inter-particle collisions), this is also shown dynamically in Supplementary Movie 1.

a way that the first element in each array always indicates the angular position for the same physical blade. This procedure is actually equivalent to blade angle linking. The first blade angle linkage is performed by following the proximity criterion  $\min[\{\theta_i(t)\} - \theta_1(t - \Delta t) \bmod 2\pi]$ .

**Step 3:** This single-feature tracking process would be enough for a naïve angular velocity detection but, since we have 14 blades, we can leverage the fact that inter-blade separation  $\Delta\theta$  is constant to increase accuracy while maintaining a low computational cost. We can now simply run a vectorized and therefore fast difference operation over the ordered angle arrays of consecutive frames, which yields the instantaneous angular displacement. In this way, the particle angular velocity  $\mathbf{w}(t)$  is

$$\begin{aligned} \mathbf{w}(t) &= \frac{\langle \Delta\theta(t) \rangle}{\Delta t} \\ &\equiv \frac{1}{\Delta t N_b} \sum_{i=1}^{N_b} [\{\theta_i(t) + \Delta t\} - \{\theta_i(t)\} \pmod{2\pi}], \end{aligned} \quad (1)$$

expression which also defines in the following the average of blades inter-frame displacement for one particle at a given time  $t$ ,  $\langle \Delta\theta(t) \rangle$ .

Although vectorization [28] does not decrease the number of operations, it allows for their computation within a common series of CPU cycles. This shrinks the execution time, in comparison with a loop of independent cross-correlations of particle images, which is the main alternative method [16]. We have empirically measured the computational complexity of our algorithm, which grows with the number of particles present in the video as  $\mathcal{O}(N)$ . We have implemented this algorithm in Python (a repository is maintained [29], the most recent version of the code is available upon request) running on an Intel® Xeon® Gold 6240 CPU @ 2.60GHz. In order to compare our execution time with that of previous works, we used 32 threads. Our tests show that we can process a realization in under 30 minutes, which is faster than cross correlation-based methods up to a factor of  $10^2$  [ ]. With further parallelization and optimizations, we are confident that this angular velocity tracking could be applied in real-time, which can be very useful for a wide variety of industrial and research applications.

We now analyze the error of angular velocity measurement for our method. In this case, error sources such as motion blur and static errors [30] (coming from lightning and camera noise) [31, 32] are negligible when compared to the main limitation of the present approach: the limited number of pixels used for detecting brightness maxima. The inner and outer radii of the annulus where brightness profiles  $B_i(\theta)$  are measured (Figure 2a) are  $r_{\text{in}} = 15$  px and  $r_{\text{out}} = 23$  px respectively (in units of image pixel length), which means that the brightness annulus occupies  $N_p = 955$  pixels (see Figure 2a), each corresponding to a different

value of  $\theta$ . As a consequence, the complete angle interval ( $2\pi$ ) is subdivided into 955 segments (the ones defined by the set of angle points in Figure 2b). Therefore, the angle resolution is, at best:  $\delta\theta = 2\pi/N_p$ . This implies that the error of the average of the inter-frame differences over all blades angles ( $\langle \Delta\theta(t) \rangle$ ) is  $\delta\langle \Delta\theta \rangle = \sqrt{\frac{2}{N_b} \frac{2\pi}{N_p}} = \pm 3.5 \times 10^{-3}$  rad. This yields an error relative to a blade section of  $\delta\langle \Delta\theta \rangle / (2\pi/N_b) = 0.78\%$ , a value that for our purpose is quite satisfactory.

This measurement error can be further reduced by using a moving average [31] up to a limit that does not result in excessive subsampling error (see Supplementary Material of our previous work [20] for more details on this). Additionally, following the common procedure in PTV techniques [5] where the central point of a particle is evaluated from a gaussian fitting of the brightness profile (thus obtaining sub-pixel accuracy), the formerly discussed relative error could be further reduced by interpolating each feature intensity distribution to effectively achieve subpixel accuracy in the determination of its position  $\theta$ . Since the error in our measurements is relatively small, we have not refined the measurement with these two additional steps in the present work.

Finally, the reader can visually check the accuracy of the method in Supplementary Movie 1 [23]. In this experimental movie, a mark that tracks the detected angle resulting from our algorithm is dynamically superimposed on each particle. It is noticeable for instance that particle spin sign reversals are detected with no error.

## 4. Results and Discussion

We have performed experiments with different number of particles in our constant area set-up, which allows for variation of particle density, which can be quantified by means of the packing fraction  $\phi = N \frac{\sigma^2}{L^2}$ .

Since in general the steady base states in our system should have polar symmetry [24], it is convenient to look at the radial profile of the average fields. In particular, we analyze here the spin velocity field  $\Omega(r) = \langle \mathbf{w} \rangle$ , and its spatial average,  $\bar{\Omega} = \langle \Omega(r) \rangle_r$ .

In Figure 3(a), we observe that  $|\bar{\Omega}|$  increases as the average kinetic energy  $\bar{T}_t$  is increased. This is expected as the torque exerted on the spinner blades must increase for higher air currents. However, it can also be seen that the variation of  $|\bar{\Omega}|$  depends on particle density. In particular, the denser the system, the slighter the increase of average spin, which can be explained by noting that the system needs more energy input in order to balance higher energy sink due to higher (inelastic) collision frequency [20]. Results reveal in Figure 3(b) that the field  $|\Omega(r)|$ , at low  $\bar{T}_t$  (blue colored data), increases monotonically vs.  $r$ , and attains its maximum value at the system boundaries. However, at higher  $\bar{T}_t$  (red), particle spin profile flattens, displaying a nearly constant value across all radii. This value is found to be proportional to  $\bar{T}_t$ . This may be due to the

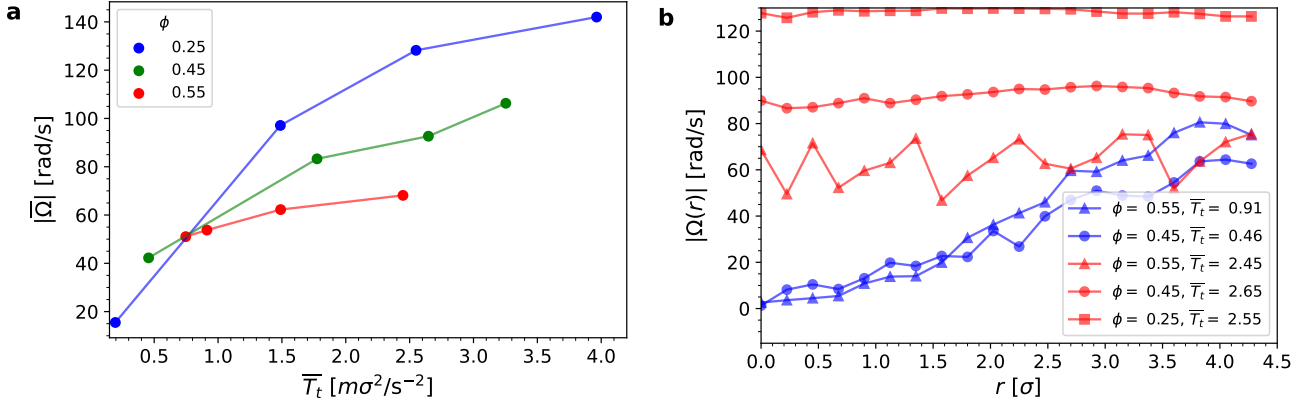


Figure 3: (a) Dependence of the average angular velocity with translational temperature; generally, mean rotational speed increases with the kinetic energy (which can be controlled by elevating the air upflow) but this figure also shows that the gradient of this growth is inversely proportional to the system density. (b) Radial profile of the mean angular velocity for different configurations of density  $\phi$  and temperature  $\bar{T}_t$  (in units of  $m\sigma^2/s^{-2}$ ). We see that there are two different regimes: when the thermalization is low, the system displays a steep radial gradient, with particles near the center having much smaller angular velocities (due to frequent collisions). Meanwhile, at higher temperatures the particles show a constant spin velocity throughout the entire system, its value being highly dependent on the packing fraction, which suggests that dissipative interactions are more frequent the higher the density.

fact that at low thermalization the density of disks tends to be higher near the center [24]. As we explained, increased density results in more frequent inter-particle collisions, which decreases (due to inelastic dissipation)  $|\Omega(r)|$ , thus preventing diffusion to outer regions [24]. However, as air power is increased (which results in higher  $\bar{T}_t$  [24]) particle spin recovers more rapidly after collisions, thus yielding a nearly constant  $|\Omega(r)|$  field. The rotational behaviour of particles, when coupled with their stochastic translational movement, play a crucial role in the development of chiral flows in this active matter system [24].

We also studied the temporal ensemble spin autocorrelation function [33], which is defined as:

$$A_{\mathbf{w}}(\tau) = \frac{\langle \mathbf{W}(t) \cdot \mathbf{W}(t + \tau) \rangle_{r,t}}{\langle \mathbf{W}(t) \cdot \mathbf{W}(t) \rangle_{r,t}}, \quad (2)$$

where  $\mathbf{W}(t) = \mathbf{w}(t) - \langle \mathbf{w} \rangle = \mathbf{w}(t) - \boldsymbol{\Omega}$  is the peculiar spin velocity, subtracting the non-zero mean spin velocity field  $\boldsymbol{\Omega} \neq 0$  caused by the constant airflow input. The  $\langle \cdot \rangle_{r,t}$  symbol in the numerator and denominator indicates that an ensemble averaging is carried out over all particles and initial times, restricting those to  $t < t_{\max} - \tau$ , where  $t_{\max}$  is the movie length. Since  $\boldsymbol{\Omega} \neq 0$  and taking into account (2), it is expected that the values of the angular autocorrelation increase in collisions, opposite to that observed in the case of the translational velocity, where the collisions rapidly decrease this value.

We plot in Figure 4(a) the time behaviour of the spin autocorrelation function,  $A_{\mathbf{w}}(\tau)$ , for two different thermalization levels. It is clear that our new measurement method captures in great detail the characteristic behavior of  $A_{\mathbf{w}}(\tau)$  [34, 35, 36]. At short times small oscillations are observable (see inset), which are generated by the tendency of the particles to revert to the average spin speed imposed by the upflow. Interestingly the frequency of these oscillations

for the two different thermalizations (considered as the inverse of the time between two consecutive maxima), is proportional to the mean spin angular velocity. We can also see that  $A_{\mathbf{w}}(\tau)$  takes higher values for the experiment with a lower thermalization level, which should be related to fact that low thermalization in this system usually implies higher density (and thus a higher collisional rate) in the system center [24]. This tends to cool down the rotational modes and thus yields a lower  $|\Omega(r)|$  field value in the central area of the experimental system, shown in Figure 3(b). Therefore, a different behavior is expected between the external and internal zone of the system. For this reason, in Figure 4(b) we split  $A_{\mathbf{w}}(\tau)$  into two zones depending on the distance of the particles to the center, one external  $r > R/2$  and the other internal  $r \leq R/2$ , ( $R = L/2$ ) being tracked the discs in each zone separately.

For the case of lower thermalization and typical collision times ( $\sim 1 - 2$  s.),  $A_{\mathbf{w}}(\tau)$  relaxes more slowly in the interior zone than in the exterior. This is due to the increased collisional effect on the inside versus dissipation on the outside edge, resulting in positive chirality in the system. On the other hand, for a greater thermalization of the discs, just the opposite occurs, the  $A_{\mathbf{w}}(\tau)$  curve relaxes faster for the internal zone compared to the external one, favoring the  $|\Omega(r)|$  field value observed and a negative chirality of the system.

In conclusion, we have presented an algorithm that accurately detects the properties of fast dynamics in a system of 2D active spinners. Furthermore, this particle tracking method can easily be adapted for angular velocity measurements for its use in an analogous particulate system, as long as its constituents have periodical features. Additionally, our algorithm has been proven to be comparatively fast and light, while retaining a high level of accuracy (our error estimation is well below 1%). Moreover,

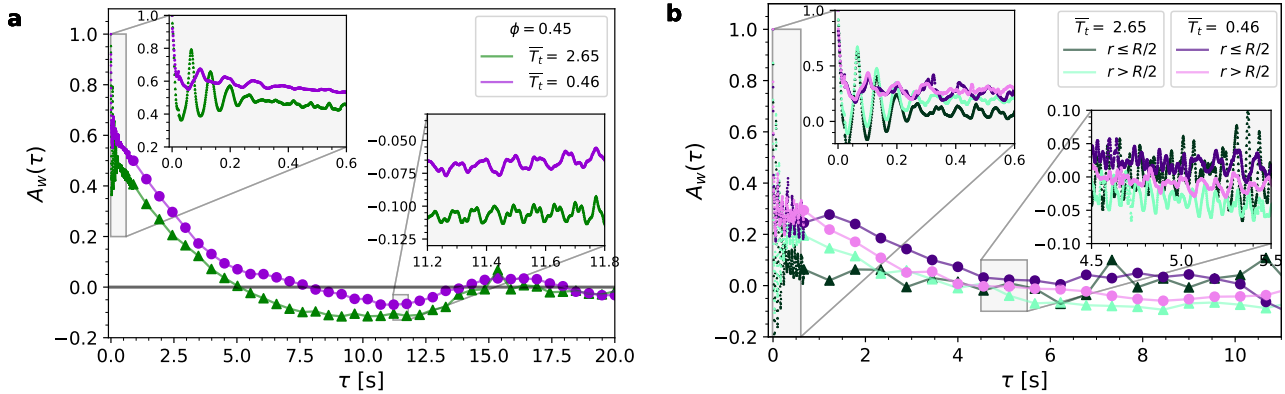


Figure 4: (a) Spin autocorrelation function, it measures the degree of similarity between angular velocity for a single particle at two instants separated by a period  $\tau$ . We compare two cases with the same density but different translational kinetic energies ( $T_t$  in units of  $m\sigma^2s^{-2}$ ). Our results demonstrate that spin autocorrelation is different inside the system with respect to the outer edge and that this behavior is reversed when thermalization varies, confirming a change in the total chirality observed in the system.

we have been able to detect rapid oscillations in the spin autocorrelations function, which poses an interesting physical problem, to be explored more deeply in a forthcoming work [37].

## Acknowledgments

We acknowledge funding from the Government of Spain through projects No. FIS2016-76359-P, PID2020-116567GB-C22 and from the regional Extremadura Government through projects No. GR18079 & IB16087, both partially funded by the ERDF. A.R.-R. also acknowledges financial support from Consejería de Transformación Económica, Industria, Conocimiento y Universidades de la Junta de Andalucía through post-doctoral grant no. DC00316 (PAIDI 2020), co-funded by the EU Fondo Social Europeo (FSE).

## References

- [1] F. Vega Reyes, A. Santos, G. M. Kremer, Role of roughness on the hydrodynamic homogeneous base state of inelastic spheres, *Phys. Rev. E* 89 (2014) 020202(R).
- [2] L. Labous, A. D. Rosato, R. N. Dave, Measurements of collisional properties of spheres using high-speed video analysis, *Physical Review E - Statistical Physics, Plasmas, Fluids, and Related Interdisciplinary Topics* 56 (5) (1997) 5717–5725. doi:10.1103/PhysRevE.56.5717.
- [3] Z. Jiang, J. Du, C. Rieck, A. Bück, E. Tsotsas, PTV experiments and DEM simulations of the coefficient of restitution for irregular particles impacting on horizontal substrates, *Powder Technology* 360 (2020) 352–365. doi:10.1016/j.powtec.2019.10.072.
- [4] P. Tierno, A. Snezhko, Transport and Assembly of Magnetic Surface Rotors\*\*, *ChemNanoMat* (2021) 1–14doi:10.1002/cnma.202100139.
- [5] J. C. Crocker, D. G. Grier, Methods of Digital Video Microscopy for Colloidal Studies, *Journal of Colloid and Interface Science* 179 (1) (1996) 298–310. doi:10.1006/jcis.1996.0217. URL <https://linkinghub.elsevier.com/retrieve/pii/S0021979796902179>
- [6] H.-Y. Lee, I.-S. Hsu, Particle Spinning Motion during Saltating Process, *Journal of Hydraulic Engineering* 122 (10) (1996) 587–590. doi:10.1061/(asce)0733-9429(1996)122:10(587).
- [7] C. Lu, R. Zhu, F. Yu, X. Jiang, Z. Liu, L. Dong, Q. Hua, Z. Ou, Gear rotational speed sensor based on FeCoSiB/Pb(Zr,Ti)O<sub>3</sub> magnetoelectric composite, *Measurement: Journal of the International Measurement Confederation* 168 (May 2020) (2021) 108409. doi:10.1016/j.measurement.2020.108409. URL <https://doi.org/10.1016/j.measurement.2020.108409>
- [8] C. Scholz, S. Jahanshahi, A. Ldov, H. Löwen, Inertial delay of self-propelled particles, *Nature Communications* 9 (1) (2018). arXiv:1807.04357, doi:10.1038/s41467-018-07596-x. URL <http://dx.doi.org/10.1038/s41467-018-07596-x>
- [9] Y. Grasselli, G. Bossis, R. Morini, Translational and rotational temperatures of a 2D vibrated granular gas in microgravity, *European Physical Journal E* 38 (2) (2015). doi:10.1140/epje/i2015-15008-5.
- [10] M. Workamp, G. Ramirez, K. E. Daniels, J. A. Dijkstra, Symmetry-reversals in chiral active matter, *Soft Matter* 14 (27) (2018) 5572–5580. doi:10.1039/c8sm00402a. URL <http://dx.doi.org/10.1039/C8SM00402A>
- [11] D. Barros, B. Hiltbrand, E. K. Longmire, Measurement of the translation and rotation of a sphere in fluid flow, *Experiments in Fluids* 59 (6) (2018) 1–14. doi:10.1007/s00348-018-2549-5. URL <http://dx.doi.org/10.1007/s00348-018-2549-5>
- [12] R. Zimmermann, Y. Gasteuil, M. Bourgoïn, R. Volk, A. Pumir, J. F. Pinton, Tracking the dynamics of translation and absolute orientation of a sphere in a turbulent flow, *Review of Scientific Instruments* 82 (3) (2011). doi:10.1063/1.3554304.
- [13] T. Hagemeier, A. Bück, E. Tsotsas, Estimation of particle rotation in fluidized beds by means of PTV, *Procedia Engineering* 102 (2015) 841–849. doi:10.1016/j.proeng.2015.01.202. URL <http://dx.doi.org/10.1016/j.proeng.2015.01.202>
- [14] R. Y. Tsai, A Versatile Camera Calibration Technique for High-Accuracy 3D Machine Vision Metrology Using Off-the-Shelf TV Cameras and Lenses, *IEEE Journal on Robotics and Automation* 3 (4) (1987) 323–344. doi:10.1109/JRA.1987.1087109.
- [15] R. J. Adrian, Particle-Imaging Techniques for Experimental Fluid Mechanics, *Annual Review of Fluid Mechanics* 23 (1) (1991) 261–304. doi:10.1146/annurev.fl.23.010191.001401. URL <http://www.annualreviews.org/doi/10.1146/annurev.fl.23.010191.001401>
- [16] N. S. Helminiak, D. S. Helminiak, V. Cariapa, J. P. Borg, Resolving the angular velocity of two-dimensional particle interactions induced within a rotary tumbler, *Journal of Visualization* 21 (5) (2018) 779–793. doi:10.1007/s12650-018-0495-1. URL <https://doi.org/10.1007/s12650-018-0495-1>
- [17] A. Papoulis, *The Fourier Integral and Its Applications*, Mcraw-Hill, New York, 1978.
- [18] R. Shnapp, E. Shapira, D. Peri, Y. Bohbot-Raviv, E. Fattal, A. Liberzon, Extended 3D-PTV for direct measurements

- of Lagrangian statistics of canopy turbulence in a wind tunnel, *Scientific Reports* 9 (1) (2019) 1–13. [arXiv:1806.04975](https://arxiv.org/abs/1806.04975), [doi:10.1038/s41598-019-43555-2](https://doi.org/10.1038/s41598-019-43555-2).
- [19] S. Farhadi, S. Machaca, J. Aird, B. O. Torres Maldonado, S. Davis, P. E. Arratia, D. J. Durian, Dynamics and thermodynamics of air-driven active spinners, *Soft Matter* 14 (27) (2018) 5588–5594. [doi:10.1039/c8sm00403j](https://doi.org/10.1039/c8sm00403j).
- [20] M. A. López-Castaño, J. F. González-Saavedra, A. Rodríguez-Rivas, E. Abad, S. B. Yuste, F. Vega Reyes, Pseudo-two-dimensional dynamics in a system of macroscopic rolling spheres, *Physical Review E* 103 (4) (2021) 042903. [arXiv:2006.15133](https://arxiv.org/abs/2006.15133), [doi:10.1103/PhysRevE.103.042903](https://doi.org/10.1103/PhysRevE.103.042903).  
URL <https://link.aps.org/doi/10.1103/PhysRevE.103.042903>
- [21] M. V. Dyke, *An Album of Fluid Motion*, Parabolic Press, Stanford, 1982.
- [22] H. Tennekes, J. L. Lumley, *A First Course in Turbulence*, The MIT Press, Cambridge, Massachusetts, 1972.
- [23] M. A. Lopez-Castaño, A. Marquez Seco, A. Rodriguez-Rivas, F. Vega Reyes, Fast measurement of angular velocity in air-driven flat rotors with periodical features - Supplementary Data (Jul. 2021). [doi:10.5281/zenodo.5141571](https://doi.org/10.5281/zenodo.5141571).  
URL <https://doi.org/10.5281/zenodo.5141571>
- [24] M. A. López-Castaño, A. M. Seco, A. M. Seco, A. Rodríguez-Rivas, F. Vega Reyes, Chirality transitions in a system of active flat spinners, preprint in [arXiv:2105.02850](https://arxiv.org/abs/2105.02850) (2021).
- [25] G. Bradski, *The OpenCV Library*, Dr. Dobb's Journal of Software Tools (2000).
- [26] M. A. L.-C. no, J. F. González-Saavedra, A. Rodríguez-Rivas, F. Vega-Reyes, *Traffic and Granular Flow 2007*, Vol. 252 of Springer Proceedings in Physics, Springer Nature, Switzerland, 2009, pp. 397–403.
- [27] D. Allan, C. van der Wel, N. Keim, T. A. Caswell, D. Wieker, R. Verweij, C. Reid, L. Grueter, *soft-matter/trackpy: Trackpy v0.4.2 (Version v0.4.2)* (2019). [doi:http://doi.org/10.5281/zenodo.3492186](https://doi.org/10.5281/zenodo.3492186).
- [28] S. Van der Walt, M. Aivazis, *The NumPy Array: A Structure for Efficient Numerical Computation*, *Computing in Science & Engineering*, *Computing in Science and Engineering* 13 (2) (2011) 22–30.  
URL <http://aip.scitation.org/doi/abs/10.1109/MCSE.2011.37>
- [29] F. Vega Reyes, M. Lopez-Castaño, A. Marquez Seco, Angular tracking source code, <https://github.com/fvegar/blades/> (2021).
- [30] T. Savin, P. S. Doyle, Static and dynamic errors in particle tracking microrheology, *Biophysical Journal* 88 (1) (2005) 623–638. [doi:10.1529/biophysj.104.042457](https://doi.org/10.1529/biophysj.104.042457).  
URL <http://dx.doi.org/10.1529/biophysj.104.042457>
- [31] Y. Feng, J. Goree, B. Liu, Errors in particle tracking velocimetry with high-speed cameras, *Review of Scientific Instruments* 82 (5) (2011). [arXiv:1104.3540](https://arxiv.org/abs/1104.3540), [doi:10.1063/1.3589267](https://doi.org/10.1063/1.3589267).
- [32] A. Sciacchitano, Uncertainty quantification in particle image velocimetry, *Measurement Science and Technology* 30 (9) (2019) ab1db8. [doi:10.1088/1361-6501/ab1db8](https://doi.org/10.1088/1361-6501/ab1db8).  
URL <https://doi.org/10.1088/1361-6501/ab1db8>
- [33] M. P. Allen, D. J. Tildesley, *Computer Simulation of Liquids*, Oxford University Press, 2017. [doi:10.1093/oso/9780198803195.001.0001](https://doi.org/10.1093/oso/9780198803195.001.0001).
- [34] B. Berne, Hydrodynamic Theory of the Angular Velocity Autocorrelation Function, *The Journal of Chemical Physics* 56 (1972) 2164.
- [35] C. Lowe, D. Frenkel, A. Masters, Long-time tails in angular momentum correlations, *The Journal of Chemical Physics* 103 (1995) 1582.
- [36] T. Lokotosh, N. Malomuzh, K. Shakun, Nature of oscillations for the autocorrelation functions for translational and angular velocities of a molecule., *Journal of Molecular Liquids* 96 (2002) 245—263.
- [37] A. Rodríguez-Rivas, M. A. López-Castaño, F. Vega Reyes, Cor-
- relations and diffusion in a chiral fluid of 2D active spinners, in preparation (2021).